



Impacts on Embankments, Rigid and Flexible Barriers Against Rockslides: Model Experiments vs. DEM Simulations

Simon Matthias Berger¹ · Robert Hofmann¹ · Alexander Preh²

Received: 6 December 2022 / Accepted: 8 December 2023
© The Author(s) 2024

Abstract

As a result of climate change, rockfalls and rock avalanches as well as landslides lead to an increasing hazard for settlement areas and infrastructures. The hazards of such mass movements mean that numerous protective structures must be planned and built. In addition to building such constructions, the refurbishment of existing protective structures is also playing an increasingly important role. Some of these protective structures are rigid structures consisting of concrete and/or steel elements. Due to the difficult accessibility, flexible net constructions are often considered. Embankment constructions are normally erected to protect against large mass movements. The choice of the right type of construction is based not only on geotechnical and geographical conditions, but also on the occurring energies and the impact of rockslides on the protective structure. In this study, small-scale laboratory experiments with different protective structures are presented. Rigid and flexible structures as well as reinforced embankments are investigated. Based on the results of the experiments, the impacts and deformations are recalculated numerically using the discrete element method (DEM). From the small-scale laboratory experiments and numerical simulations, the differences regarding the construction type of the protective structure can be investigated. An essential main point concerns the relationship between the flexibility of the barrier and the total impact load. The presented work is limited to the investigation of strongly fragmented gravitational mass movements such as rock avalanches.

Highlights

- The results from model experiments are shown and analyzed to investigate the impacts on protective structures due to highly fragmented granular mass movements (rock avalanches).
- The behavior of protective structures, such as rigid barriers, flexible barriers, and embankments, is investigated.
- Numerical simulations based on the discrete element method (DEM) are used to calculate the flow characteristics of the granular mass, the force–time behavior of the impact on the different types of barriers, and the deformations of the flexible barriers.
- Based on the model experiments and DEM simulations, a limit value is determined depending on the deformation, at which an increased load on flexible protective structures should be taken into account.

Keywords Rock avalanches · Model experiment · DEM simulation · Rigid barriers · Flexible barriers · Embankments

1 Introduction

Both the expansion of settlement areas and climate change increase the hazards posed by gravitational mass movements. According to Gariano and Guzzetti (2016) and Gobiet et al. (2014), increasing temperatures and more intensive precipitation events will increase the occurrence of gravitational mass movements in future. For protection against gravitational natural hazards, cost-intensive protective structures are generally built. For the design

✉ Simon Matthias Berger
simon.berger@uibk.ac.at

¹ Unit of Geotechnics, Faculty of Engineering Sciences, University of Innsbruck, Technikerstraße 13, 6020 Innsbruck, Austria

² Research Unit of Engineering Geology, Institute of Geotechnics, Vienna University of Technology, 1040 Vienna, Austria

of protective structures against rockfall or debris flow in Austria, standards and regulations have been put in place, such as the Austrian national regulations (ONR 24800 2009; ONR 24802 2011; ONR 24801 2013; ONR 24810 2021). There are no standards or regulations for actions resulting from large granular mass movements, such as rock avalanches. The modeling, according to ONR, for debris flows can nevertheless be used as a basis for the formation of an impact model. If the impacts are considered in the form of forces and pressures, various authors (Vagnon and Segalini 2016; VanDine 1996; Canelli et al. 2012), analogous to the ONR, separate the dynamic impact (F_{dyn} or p_{dyn}) from the static load (F_{stat} or p_{stat}). In Li et al. (2021), a combination of dynamic impacts and static loads was recommended. If the force–time history on a protective structure is investigated, the maximum impact (F_{dyn} or p_{dyn}) is designated as dynamic. The static load (F_{stat} or p_{stat}) results in the final state when the granular mass in front of the protective structure is at rest. The term “static” does not refer to a substitute force of the dynamic action, but to the force that results at the end of the process due to the dead zone. From a mechanical point of view, the term “residual” would be more appropriate instead of “static”. According to the ONR, Ashwood and Hungr (2016) or Poudyal et al. (2019), the dimensioning decisive dynamic impact on the protective structure can be calculated from the parameters of the process model, (see Fig. 1).

The static pressure (p_{stat}) in Eq. 1 can be determined with the static deposition height (h_{st}), density (ρ), gravity (g) and dimensionless coefficient (K). The dynamic pressure (p_{dyn}) in Eq. 2 can be determined with the density (ρ), velocity (v) and dynamic coefficient (α).

The static pressure (p_{stat}) on a protective structure due to a granular mass is determined as follows:

$$p_{\text{stat}} = K \cdot h_{\text{st}} \cdot \rho \cdot g \quad (1)$$

The dynamic impact pressure (p_{dyn}) on a protective structure due to a granular mass impact is determined as follows:

$$p_{\text{dyn}} = \alpha \cdot \rho \cdot v^2 \quad (2)$$

If the width (b) and deposit height (h_{st}) are taken into account, the static force (F_{stat}) can be determined from the static pressure (p_{stat}). If the width (b) and flow height (h_{f}) are taken into account, the dynamic impact force (F_{dyn}) can be determined from the dynamic impact pressure (p_{dyn}). The ratio of the vertical to horizontal stresses is considered via the dimensionless coefficient (K). Equation 2 is based on the momentum theorem and assumes knowledge of the parameters in the process model (Fig. 1). In general, the approaches are based on the determination of the actions due to debris flows. A derivation of empirical factors for rock avalanches is in principle conceivable and has been investigated by various authors (Hungr et al. 1984; Daido 1993; Bugnion et al. 2012; Canelli et al. 2012). A general summary of different dynamic coefficients (α) was published by Poudyal et al. (2019). Measurements on real protective structures due to the impact of rock avalanches generally fail due to the size of the mass movement of rock avalanches. The determination of the impact of such granular mass movements as well as the determination of the empirical factors (K) and (α) in Eqs. 1 and 2 is mostly derived from small-scale laboratory experiments. Taking into account the model laws (1-g model law or Froude’s model law), the conclusions from those experiments can be applied to real protective structures (Berger and Hofmann 2022; Lambert et al. 2023; Cagnoli 2021). In general, small-scale laboratory experiments have been studied to investigate the impacts on rigid barriers, such as by Moriguchi et al. (2009), Proske et al. (2011) and Jiang and Towhata (2013). Small-scale laboratory experiments for the investigation of flexible barriers were conducted by Ashwood and Hungr (2016) and Wendeler et al. (2019). Studies on rigid and flexible barriers using centrifuge models were conducted by Ng et al. (2017). A numerical analysis of a single impact (rockfall) was investigated by Volkwein (2005). An empirical approach derived from small-scale laboratory experiments to determine the impacts due to rock avalanches can be found in Hofmann and Berger (2022). In Poudyal et al. (2019), recommended values by different authors for the dynamic coefficient (α) were published. Values for (α) were between 1.0 and 5.0. In Ng et al. (2021), the calculation of (α) as a function of the Froude number (Fr) was recommended. The values recommended for (α) were thus derived purely empirically or as a function of the flow parameters according to Fig. 1. In general, however, the impacts are considered independently from the type of protective structure. Numerical studies investigating

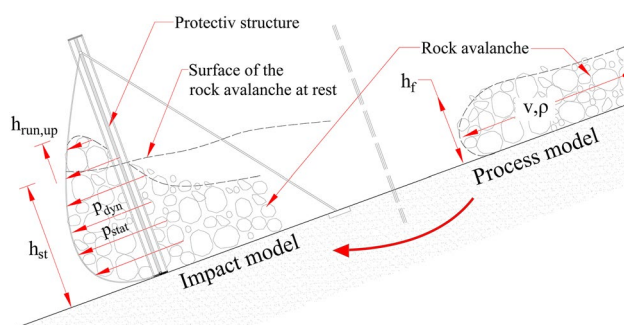


Fig. 1 Representation of the rock avalanche for the process model and the impact model. The parameters of the impact model with velocity (v), density (ρ), and flow height (h_{f}). The parameters of the impact model with dynamic impact pressure (p_{dyn}) and static load pressure (p_{stat}), deposition height (h_{st}), and the height of the run up ($h_{\text{run,up}}$)

the effects on rigid barriers due to granular masses were investigated by Jiang et al. (2018), Ashwood and Hungr (2016) and Albaba et al. (2018). Discrete element simulations of the impacts between flexible structures and granular masses were studied by Liu et al. (2020) and Albaba et al. (2017). The present study therefore deals with the effects on different types of protective structures as a result of highly fragmented, fast granular mass movements, which occur, for example, in rock avalanches. Small-scale laboratory experiments were used for the study. For the entire study in this paper, the experimental boundary conditions (except for the type of protective structures) remain unchanged. From this, the differences can be examined based exclusively on the type of barrier. One rigid barrier, three different flexible barriers, and one reinforced embankment construction were investigated as protective structures. In addition to the presentation of the experimental results, a three-dimensional discrete element model was created and used to calculate the measured experimental results.

2 Model Experiments

The model apparatus at the University of Innsbruck consists of a reservoir, a gate, a flume base, and sidewalls, all of which are shown in Fig. 2. With the exception of the sidewalls, the small-scale laboratory experiment consisted of galvanized steel (see Fig. 2). One of the side walls was made with acrylic glass, including a grid which allows geometrical interpretation of the granular mass during the flow. The length of the flume base was 3.2 m, the width (b) was 32.5 cm, and the height (h) was about 30 cm (see Fig. 3). At the lower end of the flume base, a slide on rollers was attached. The slide allows the attachment of the different barriers as well as the coupling of the barriers to the load cell.

The test procedure begins by filling the model with 25 kg of test material. The entire opening time of the flap takes

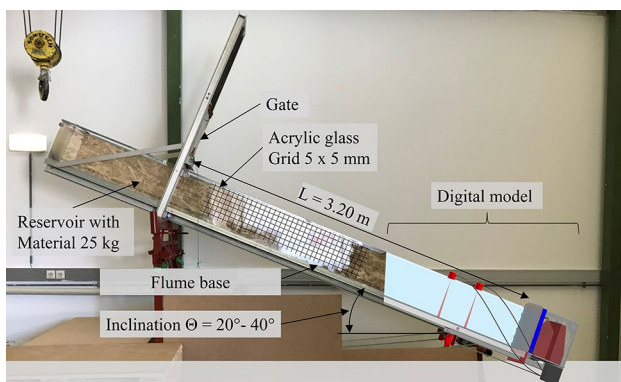


Fig. 2 Combination of the digital and photo model of the small-scale laboratory experiment at the University of Innsbruck

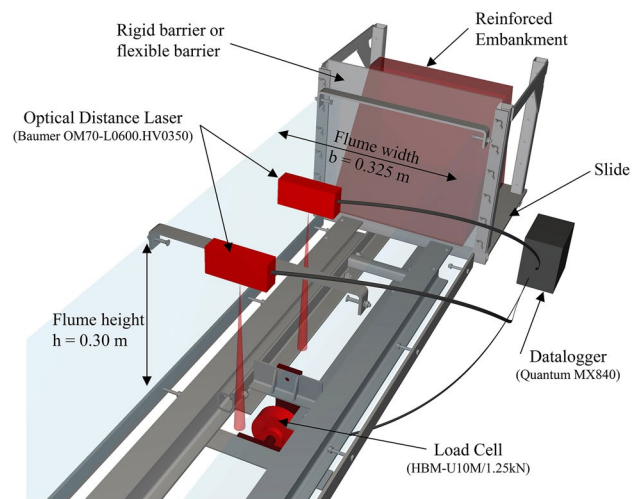


Fig. 3 Illustration of the lower part of the small-scale laboratory experiment including the measurement instrumentation (optical distance laser, load cell, and datalogger), the different types of protective structures, as well as the slide and geometric dimensions

approx. 0.2 s and was performed mechanically. When the gate is opened, the material accelerates due to gravity along the flume base until it is stopped by the barrier. During the flow of the granular mass, the velocity (v) and flow height (h_f) are of particular interest. For the measurement of these parameters, two optical distance lasers (Baumer OM70-L0600.HV0350) were installed. The measuring frequency of the distance lasers is 2500 Hz. In addition, videos were recorded using two video cameras (SONY α 6400L) at 100 fps and a resolution of 1020×720 px. The evaluation of the velocity was performed with the Kinovea[®] software. The software allows marking the front of the granular mass for each time step. As a result, a path–time diagram is generated from which the velocity can be calculated. In addition to the measurement of the flow properties of the granular mass, the measurement of the impact on the barrier is essential. All barrier types were mounted on a slide located at the end of the flume base. The slide was mounted on rollers and connected to the load cell (HBM U10M/1.25 KN). The measured force on the barrier is the total force acting on the structure in the direction parallel to the flume. The recording from the distance lasers and the load cell was synchronized by the measurement amplifier (Quantum MX840). The positioning of the measuring instruments as well as the storage of the barriers can be taken from Fig. 3.

A total of approx. 200 experiments were carried out at the University of Innsbruck between 2020 and 2022. A flume base inclination of approx. (θ) between 20° and 40° and different granular materials were used. The experimental results can be taken from Hofmann and Berger (2022). In this paper, only the results of the small-scale laboratory experiments with an inclination (θ) of 30.2° and the

material mixture were used. The choice of this test setup was due to the fact that an inclination of 30.2° lies approximately in the middle of the entire range. The test material (mixture) allows the investigation of granular masses with different grain sizes. A total of 20 experiments were conducted for this purpose. Table 1 shows the number of experiments carried out depending on the type of barrier.

2.1 Materials

A mixture of sand and gravel with a weight ratio of 1:1 was used for the experiments. The sand particles had grain sizes of 0.5–1.0 mm and the gravel grain sizes ranged from 4.0 to 8.0 mm. Figure 4 shows the particle size distribution of the sand, of the gravel, and of the mixture. In addition, the grain shape of the sand and the gravel particles can be seen in Fig. 4.

In addition to the particle size distribution, the internal friction angle (φ) of the material and the friction angle (φ_b) between the material and the flume base of the small-scale laboratory experiments was determined in the laboratory. The internal friction angle (φ) of the mixture was approx. 33.5° and was determined with the help of a bulk cone test. The basal friction angle (φ_b) was determined with tilt tests analogous to Hungr (2008). For this purpose, an acrylic glass cylinder is placed in the horizontally positioned laboratory experiment. This was then filled with the test material (mixture). Subsequently, the inclination of the model experiment was increased step by step, with a small impact on the chute after each increase (Hungr 2008). The inclination ($\varphi_{b,d}$) at which the cylinder with the mixture began to move was then measured. The same experiment without a small impact was used for the determination of ($\varphi_{b,s}$). The result is not a definite value but a range of values and serves as a guide since both the acrylic glass cylinder and the amount of mixture influence the measurement result. Without impulsive loading, a higher friction angle is measured. Performing the tests in this way prevented the individual particles from rolling because they are locked in the cylinder. As a result, the sliding friction was determined when the rolling was hindered. In addition, tipping tests with slow-motion videos were used to investigate the inclination at which the individual particles of the mixture began to roll. This angle is

Table 1 Number of experiments at the University of Innsbruck using the mixture at a flume inclination (θ) of 30.2°

Material	Rigid barrier	Flexible barriers			Reinforced embankment
		Net I	Net II	Net III	
Mixture (sand–gravel)	7	3	3	3	4

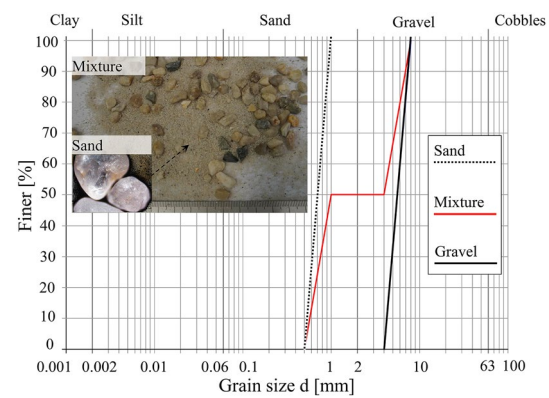


Fig. 4 Grain size distribution of the test material, sand, gravel, and the mixture, including an illustration of the grain shape

called the rolling friction angle (φ_{roll}) and gives information about the grain shape of the individual particles. The density of the mixture was approx. 1780 kg/m^3 for the loosest storage and 1872 kg/m^3 for the densest storage. In Table 2, the mean values of the laboratory tests of the parameters (φ , $\varphi_{b,d}$, $\varphi_{b,s}$, φ_{roll} , and ρ) of the mixture are listed.

2.2 Different Types of Barriers

In the laboratory experiments, three different types of barriers were investigated. One rigid barrier, three flexible barriers and one reinforced embankment construction. The three different types of barriers, including positioning in the slide, can be seen in Fig. 5.

An approx. 1 cm thick galvanized steel plate was used as a rigid barrier. The steel plate was mounted laterally on the slide at the bottom in a non-displaceable manner. For the flexible barrier, three different flexible materials were used. In the following, the flexible barriers are referred to as Net I, Net II and Net III. Net I consist of a grid of glass fibers with a mesh size of $1.5 \times 1.5 \text{ mm}$ and high stiffness. Net II

Table 2 Material parameters of the mixture

Material	Friction angle [$^\circ$]			Density
	Friction angle Particle–particle	Basal friction angle Particle–flume	Rolling friction angle Particle–flume	
	φ [$^\circ$]	$\varphi_{b,d}$ [$^\circ$] $\varphi_{b,s}$ [$^\circ$]	φ_{roll} [$^\circ$]	ρ [kg/m^3]
Mixture	33.5	21–22 ^a 23–27 ^a	~22 to 26	1780–1872

Friction angle (φ , φ_b and φ_{roll}) and bulk density (ρ) of the mixture
^aThe flume base was galvanized and was much rougher than a smooth steel surface

and Net III consist of a fabric made of cotton with varying amounts of elastane. The description of the nets based on their components provided insufficient information about their stiffness. For this reason, tensile tests were carried out at the University of Innsbruck for Net I, Net II, and Net III (see Fig. 6). The tensile tests were carried out on 2.5 cm wide and 15 cm long strips. A strip of the flexible material was fixed at the top and bottom. The AGS-X series apparatus from SHIMADZU was used to conduct the tensile tests. The loading speed was between 5 and 25 mm/min. During the tests, the change in length of the flexible material and the corresponding load were recorded. For each flexible material (Net I, Net II, and Net III), at least three tensile tests with loading rates between 1 and 7 mm/min were performed. The test results, shown in black in Fig. 6, were approximated and

linearized per section. The resulting curves are shown in Fig. 6 as Net I_{linear}, Net II_{linear}, and Net III_{linear}. Taking into account the width of 2.5 cm and the thickness of 0.3 cm, the linearized stiffness is reported for each section (see Fig. 6).

The flexible barrier in the slide in its deformed position after the test is shown on the left in Fig. 7. In the laboratory experiments, the reinforced embankment had a height of approx. 30 cm and a crown width of approx. 6 cm. The lateral inclination of the embankment was approx. 70°. The embankment was constructed in sections of 2 cm thick layers of sand. A wide-graded sand mixture with grain sizes ranging from 0.06 to 2 mm was used for the embankment. A geosynthetic net (GGR_LS) consisting of a synthetic material with a mesh size of approx. 1 mm was used to separate the individual layers. The net (GGR_LS) had a layer thickness of 0.24 mm, a

Fig. 5 Illustration of the different types of barriers; left, rigid barrier consisting of a steel plate; middle, flexible barrier in the deformed position; right, reinforced embankment construction. All barrier types were fixed to the slide

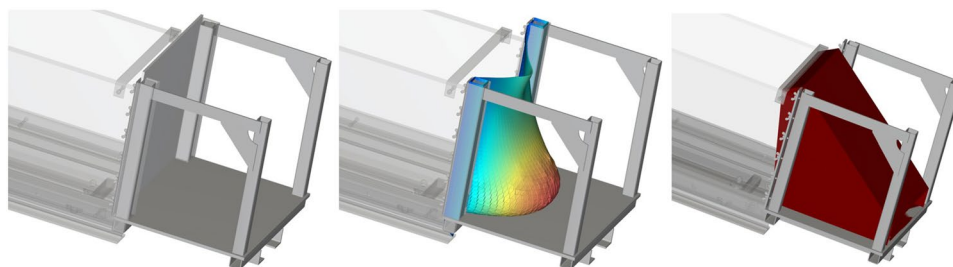


Fig. 6 The force–strain behavior of the flexible materials for a 2.5 cm width strip, adapted from Hofmann and Berger (2022). Net I_{linear}, Net II_{linear}, and Net III_{linear} indicate the approximated curves of the force–strain relationship of the individual materials

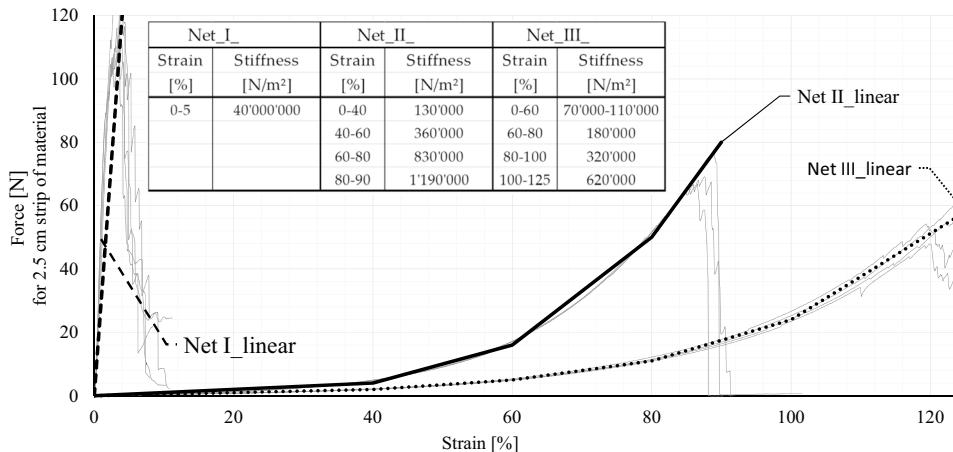


Fig. 7 Slide of the small-scale laboratory experiment with the flexible barrier, left, and the reinforced embankment, right. The Net III flexible barrier is shown in its deformed position. The reinforced embankment had a height of 30 cm, a crown width of 6 cm, and an inclination to the horizontal of approx. 70° on both sides

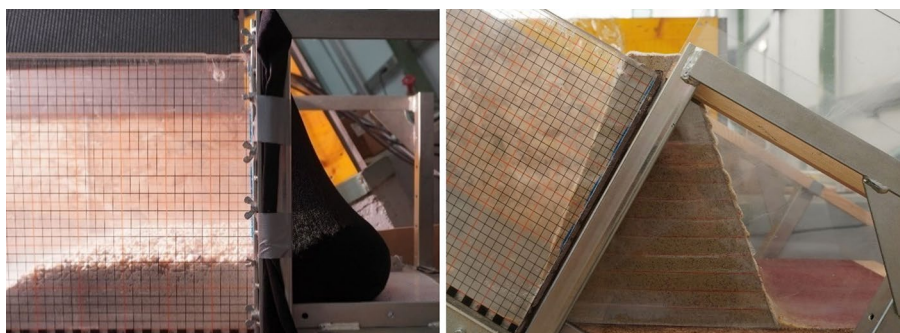


Table 3 Mean value and standard deviation (σ_{sdt}) from 20 experiments of the velocity (v), flow depth (h_f) and Froude number (Fr) of the mixture at an inclination of 30.2° before hitting the barriers

Barrier type	Flume inclination (θ)	Frontal velocity (v)	Flow depth (h_f)	Froude number (Fr)
	[$^\circ$]	[m/s]	[mm]	(–)
Rigid, flexible, reinforced embankment	30.2	$v_{\text{mean}} = 3.4$ (mean) $\sigma_{sdt} = 0.6$	$h_{f,\text{mean}} = 11.7$ $\sigma_{sdt} = 3.1$	$F_{r,\text{mean}} = 10$ $\sigma_{sdt} = 2.1$

Fig. 8 The state of the test material (mixture) during the impact process at three different times. The flow height (h_f) and static deposition height (h_{st}) are indicated

weight per unit area of 2.8 kg/m^2 , and a tensile strength of 2.94 kN/m transverse to the direction of the embankment and 1.37 kN/m along the direction of the embankment. Figure 7 (right) shows the reinforced embankment in the slide.

3 Experimental Results

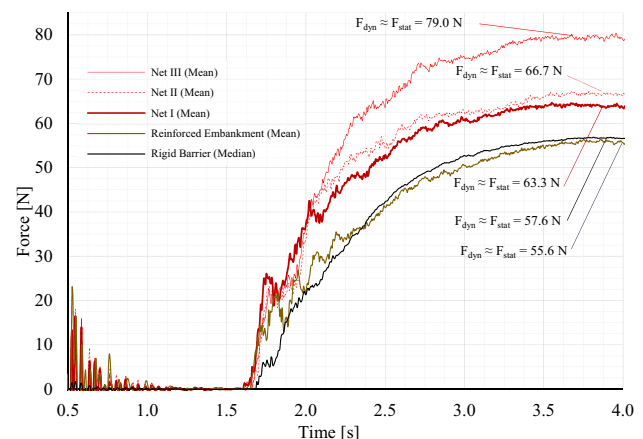
3.1 Flow Characteristic Results of the Granular Materials

For the analysis of the velocity (v) and flow height (h_f) of the granular mass (mixture), the measurement data of the two optical distance lasers and the evaluation of the video analysis were used. For the interpretation of these measurement results, the tests with the rigid barriers, flexible barriers, and the reinforced embankment can be used. A total of 20 tests with a flume base inclination (θ) of 30.2° and the test material mixture were performed for this purpose (cf. Table 1). Table 3 shows the mean values of the velocity (v) and flow depth (h_f) before hitting the barriers evaluated from all 20 experiments.

At the end of the test, the granular mass was at rest and showed significant segregation between the individual particle sizes in the mixture (Fig. 8, right). The larger gravel particles are deposited in the upper part of the mixture. The smaller sand particles lie underneath this, which slip through the larger gaps in the gravel (sieve effect). This inverse grading also occurs during the mass movement. The larger particles "float" on the surface. The same effect also occurs in the numerical simulation (see Sect. 5).

3.2 Impact Results Due to the Rigid Barriers, Flexible Barriers and Reinforced Embankments

The evaluation of the load cell measurement data (force–time history) for the different types of barriers can be seen in Fig. 9. In Fig. 9, the mean value is shown for the flexible

**Fig. 9** Evaluated measurement results as a force–time diagram for the rigid barrier, the flexible barrier (Net_I, Net_II, and Net_III), and the reinforced embankment due to the mixture at a slope inclination (θ) of 30.2° , adapted from (Hofmann and Berger 2022)

barriers and the reinforced embankment. It is important to note that the flow of the granular mass is only parallel to the flume at the beginning of the impact. Subsequently, the flow is redirected by the dead zone and by the deformation of the flexible barrier. For the force–time history of the rigid barrier, the median is shown for seven tests. The measurement recording of the load cell was initiated using a trigger point via the measurement amplifier (Quantum MX840). Opening the gate caused brief vibrations in the small-scale laboratory experiment. These vibrations caused small forces in the load cell, which were selected as the trigger point ($F > 5 \text{ N}$). This allows the different experiments to be synchronized in time. For the measurement recordings, the data were saved 0.5 s before the gate was triggered (trigger point). The influence of the vibrations caused by the opening of the gate on the barrier was negligible. The forces in the force-measuring cell were at zero immediately before the granular mass started to impact the barriers (see Fig. 9). A total of seven

test data were recorded for the rigid barrier (see Table 1), and thus the median in Fig. 9 is plotted for this test series instead of the mean value.

The difference in inclination of the impact surface between the rigid barrier and the embankment was around 10° . This is mainly because the tests were carried out at an inclination of 30.2° . This results in small differences in the force–time history between the rigid barrier and the embankment (see Fig. 9). Figure 9 clearly shows that the flexible barriers (Net I, Net II, and Net III) result in the highest forces (F_{dyn} and F_{stat}). For the flexible barriers, it is observed that the lower the stiffness, the higher the load. For the test series of the mixture with an inclination (θ) of 30.2° , Fig. 9 shows that the dynamic impact force (F_{dyn}) hardly exceeds the static force (F_{stat}) value in the final state. Table 4 shows the measured value of the impact force (F_{stat} and F_{dyn}). Because the difference between the dynamic impact force (F_{dyn}) and the static force (F_{stat}), respectively, for all experiments is less than 5%, the values in Table 4 can be set as equal. This further means that the designation dynamical (F_{dyn}) is not significant and the static force (F_{stat}) follows almost exclusively from the load due to the dead zone. For these forces, Table 4 shows the minimum ($F_{\text{stat, min}}$, $F_{\text{dyn, min}}$) and maximum values ($F_{\text{stat, max}}$, $F_{\text{dyn, max}}$) from all experiments.

3.3 Deflection Results of the Barriers

Table 5 lists the experimental results of the deposition height (h_{stat}) of the mixture and the deformation of the flexible barrier (f_{max} , see Fig. 13) when the mixture was at rest. The deposition height (h_{stat}) is the parallel distance from the flume base to the upper surface of the mixture directly in front of the barrier. To compare the deflection of the flexible barrier, the maximum deformation (f_{max}) was measured in the direction of the small-scale laboratory test (see Fig. 13). Additionally, Table 5 shows the extreme values of the deformation (f_{max}) and the static height (h_{st}). The values in parentheses in Table 5 represent the minimum and maximum measured values of all experiments. The value between the parenthesis in Table 5 represents the mean value of all experiments. For each flexible barrier, three experimental results were conducted. The variation in the measured values

Table 5 Results of the small-scale laboratory experiments at an inclination of 30.2° , listing the static deposition height (h_{st}) of the mixture in front of the barrier and the deformation (f_{max}) of the barriers when the mixture was at rest

Barrier type		Static height in front of the barrier h_{st} [cm]	Deformation of the barrier f_{max} [cm]
Rigid		(10.0)/11.1/(12.0)	–
Flexible	Net I	(10.1)/10.5/(11.0)	(4.5)/4.5/(4.6)
	Net II	(9.3)/9.6/(9.8)	(13.9)/14.0/(14.1)
	Net III	(8.7)/9.3/(10.0)	(17.2)/17.5/(17.7)
Embankment		(10.8)/11.2/(11.7)	–

of the deformation (f_{max}) was small. The largest variation for the deformation (f_{max}) was for Net III with 0.5 cm.

4 Numerical Model

The discrete element method DEM (Cundall 1971; Cundall and Strack 1979) is particularly suitable for the numerical modeling of granular flows, since it allows for the calculation of particles trajectories moving simultaneously and the simulation of particle–particle interactions (Campbell and Brennen 1985; Cao et al. 1996; Roth 2003; Preh 2020). For numerical modeling, the discrete element code Rocky@ (Version 22.2.0) from ESSS was used. To optimize the computation time, the mixture was approximated using spherical particles. The calculation time was reduced from the fact that geometrically only one parameter (radius) is needed to describe the grain shape of a particle. The number of particles in 25 kg of test material varies with particle diameter. If the real sizes of the grading curve (Fig. 4) are taken into account as particle diameters, this results in more than 20 million particles. Due to this high number of particles, the scaling factor "coarse grain" was used in the DEM simulation. Coarse Grain Modeling (CGM) represents the granular mass as larger particles. These larger particles represent a group of smaller particles of the original size. The interaction between the larger and original particle sizes is adjusted to preserve the dynamics of the original system (ESSS Rocky Release 2022 R1.2). All numerical calculations were

Table 4 Measured force values on the barriers, minimum (F_{min}) and maximum measured (F_{max}) due to the mixture under an inclination of 30.2°

Barrier type		Min value of all test results $F_{\text{stat, min}} \cong F_{\text{dyn, min}}$ [N]	Max value of all test results $F_{\text{stat, max}} \cong F_{\text{dyn, max}}$ [N]
Rigid		54.0	65.3
Flexible	Net I	62.0	66.0
	Net II	64.0	68.0
	Net III	76.0	81.0
Embankment		53.0	58.9

performed on a high-performance computing cluster (HPC) with a GPU Nvidia Tesla V100 at the University of Innsbruck. For calculations with rigid barriers, a total of approx. 4.9 million particles were used. For calculations with flexible barriers, a total of 620,000 particles were used. The reduction in the number of particles for calculations with the flexible barriers is due to the fact that additional material behavior needs to be considered for the flexible barrier. This material behavior requires additional calculation time and is explained below. The calculation time of each DEM simulation was between 15 h and 4 days. In the DEM calculation, a linear spring dashpot model was used to describe the normal forces between the particles and between the particles and the slide. For a description of the tangential forces, a linear spring dashpot model with a coulomb limit was used. The geometrically perfect spherical objects do not describe the real grain shape of the gravel and sand particles. For this reason, a rolling friction model was considered in the DEM simulation. The simulation included both the filling of the test material (mixture, 25 kg) and the opening of the gate in approx. 0.2 s. The numerical parameters describing the interaction between the particles of the mixture and the small-scale laboratory experiment were determined in the laboratory at the University of Innsbruck. These can be seen in Table 6.

The interactions in the DEM simulation between the particles of the mixture and the different barriers were taken

into account using the parameters from Table 7. Since the individual barriers in the small-scale laboratory experiment were mounted on a removable slide, the barriers could be aligned horizontally. The restitution coefficients could thus be determined in the same way as described in Table 6. The determination of the restitution coefficient, especially for the flexible barrier, corresponds to the boundary conditions in the small-scale laboratory experiment. The Poisson's ratio

Table 7 Overview of the material parameters used for the numerical calculation using the discrete element method (DEM)

Physical parameters	Unit	Value
Restitution coefficient		
Particle–rigid barrier	[-]	0.55
Particle–flexible barrier	[-]	0.2
Particle–embankment	[-]	0.3
Stiffness/Poisson's ratio		
Rigid barrier	[N/m ²]/[-]	^a / _a
Flexible barrier	[N/m ²]/[-]	100,000– 2,750,000/0.4
Embankment	[N/m ²]/[-]	^a / _a

Material parameters for the interaction between the mixture and the barriers

^aNo deformations were allowed for the rigid barrier or the reinforced embankment

Table 6 Overview of the material parameters used for the numerical calculation using the discrete element method (DEM)

Physical parameters	Unit	Value	Description of how the value was determined
Friction coefficient			
Particle–particle	[-]	0.66	The coefficient of friction between the particles was calculated from the friction angle (φ) in Table 2 $\tan(33.5^\circ) = 0.66$
Particle–flume base	[-]	0.48	The coefficient of friction between the mixture and the flume base was assumed to be 0.48. The resulting friction angle was within the range of the measured values in Table 2 $\tan(25.6^\circ) = 0.48$ No differences between the static and dynamic friction coefficients, analogous to Matuttis and Chen (2014), were considered
Tangential stiffness ratio	[-]	1.00	Taken as 1, since there was no expected difference in the effect between the normal and tangential stiffness
Restitution coefficient			
Particle–particle	[-]	0.15	Restitution coefficient was determined with drop tests from the energy balance with the following formula: $\sqrt{\text{Height}_{\text{afterimpact}}/\text{Height}_{\text{beforeimpact}}}$ To determine the coefficient of restitution, the particles were dropped from a height of 50 cm. Using the slow-motion recordings, the rebound height after hitting the galvanized steel surface can be determined. Similarly, a layer of mixture was used in place of the galvanized steel surface. The values determined in this way are to be understood more as guide values and not as mechanically precise measurable values. In particular, the interpretation of the rebound height from the slow-motion recordings is unclear. Furthermore, the particles rarely bounce vertically upwards after impact Height before impact = 50 cm; Height after impact = 1–2 cm Height before impact = 50 cm; Height after impact = 15–17 cm
Particle–slide	[-]	0.55	
Rolling resistance	[-]	0.45	The coefficient of rolling friction was estimated for an inclination of about 22°–26° (see Table 2)

Material parameters for the interaction between the mixture and the small-scale laboratory experiment

in Table 7 is based on an assumption and was roughly estimated from the tensile tests.

The rigid barrier and the reinforced embankment were implemented into the DEM simulation as unmoveable geometric boundary conditions (see Table 7). For the flexible barriers, this assumption did not apply. In order to model large displacements or deformations, the flexible barriers were modeled with a "flexible shell". Essentially, the "flexible shell" describes a connected polygon mesh of individual, connected particles. The particles within the polygon mesh of the flexible barriers are referred to as elements. The elements themselves are not deformable. Neighboring elements are connected to each other and can move in translation or twist in relation to each other. The flexibility, thus, results exclusively in the description of the behavior between the elements (joints). In response to the displacement or twisting, a joint between the elements reacts with forces and moments (see Fig. 10) that counteract the deformation. The elements have a constant thickness. The thickness of the flexible barriers was 0.3 cm. In Fig. 10, the forces (F_n, F_τ), moments (M_T, M_{B1}, M_{B2}), displacements (d_n, d_τ), and angles ($\Theta_T, \Theta_{B1}, \Theta_{B2}$) of two adjacent elements are shown (ESSS Rocky Release 2022 R1.2).

A linear elastic model was used to describe the interaction of two neighboring elements. The general equations for describing the behavior between the two elements, which are shown in Fig. 10, can be taken from the software manual (ESSS Rocky Release 2022 R1.2). The discretization of the flexible barrier was conducted using the computer program Rhino® (version 6 SR35 2021-8-10) with triangular elements. The simulation with flexible elements without a viscous damping model would lead to endless oscillations. To counteract this situation, the following viscous damping model was used with the forces (F_n^v, F_τ^v) and moments ($M_T^v, M_{B1}^v, M_{B2}^v$) which are considered to reduce the internal vibrations of the flexible elements. The forces (F_n^v, F_τ^v) were obtained as a function of the damping coefficient (C_n, C_τ) and the relative normal or tangential velocity (v_n^{rel}, v_τ^{rel}) of the connected elements according to Eq. 3.

$$F_n^v = C_n \cdot v_n^{rel}, F_\tau^v = C_\tau \cdot v_\tau^{rel} \tag{3}$$

The moments ($M_T^v, M_{B1}^v, M_{B2}^v$) were obtained analogously to Eq. 3, taking into account the relative angular velocity ($w_T^{rel}, w_{B1}^{rel}, w_{B2}^{rel}$) of the connected elements according to Eq. 4.

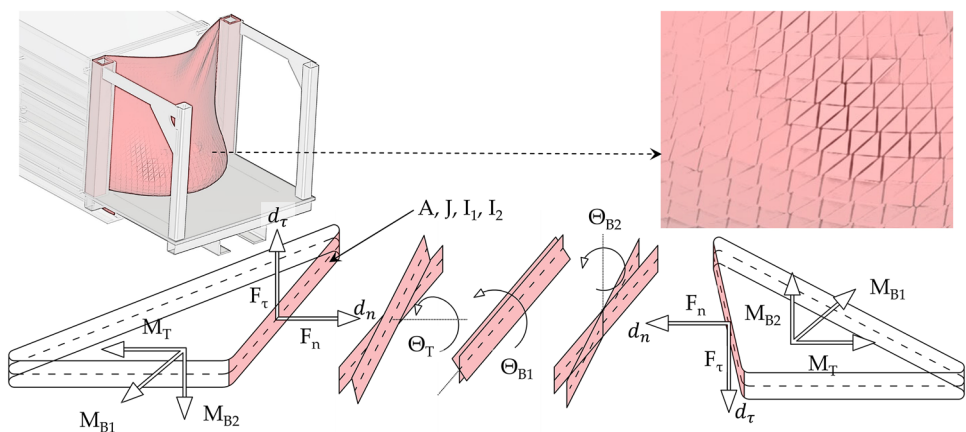
$$M_T^v = C_\tau \cdot \frac{J}{A} \cdot w_T^{rel}, M_{B1}^v = C_n \cdot \frac{I_1}{A} \cdot w_{B1}^{rel}, M_{B2}^v = C_n \cdot \frac{I_2}{A} \cdot w_{B2}^{rel} \tag{4}$$

The normal and tangential damping coefficients (C_n, C_τ) were calculated using Eq. 5.

$$C_n = 2\eta\sqrt{m \cdot K_n}; C_\tau = 2\eta\sqrt{m \cdot K_\tau} \tag{5}$$

In Eq. 5, (η) denotes a unitless damping parameter and (m) the mass of the elements. The damping parameter (η) is generally between 0 and 1. The higher the value, the faster the vibrations decay. When determining the effects on the flexible barrier due to the gravitational mass in the force–time history, the unitless damping parameter (η) does not play a significant role. In the DEM simulation, $\eta = 0.2$ was used. This ensures that the flexible barriers do not oscillate infinitely at the end of the simulation. At this point, it should be mentioned that the unitless damping parameter (η) must not be confused with the restitution coefficient in Table 6 or 7. The damping parameter (η) serves to specifically avoid endless oscillations between the elements. In the DEM simulation, values between $0.1 < \eta > 0.75$ were investigated, and the influence for the maximum force (F_{dyn}) was lower than 1%. In contrast to the rigid barrier, the modeling of the flexible barrier was possible with the stiffness (E), Poisson's ratio (P), and geometric dimensions of the flexible barrier.

Fig. 10 Discretization of the flexible barrier with triangular elements. Description of the interaction between the elements with the displacement (d_n, d_τ) and rotation ($\Theta_T, \Theta_{B1}, \Theta_{B2}$) and the associated forces (F_n, F_τ) and moments (M_T, M_{B1}, M_{B2})



5 Comparison Between the Numerical and Experimental Results

5.1 Results of the Flow Characteristics of the Granular Material (Mixture)

The measurement results of the small-scale laboratory experiments for the velocity (v) and flow height (h_f) of the mixture before the granular mass interacts with the barriers are listed in Table 3. The parameters in Tables 6 and 7 were used for the DEM simulation. Figure 11 (left) compares the velocity (v) and flow height (h_f) between the measurement results from the model experiments and the DEM simulation. The analysis of the velocity (v) of the mixture varies from place to place and from particle to particle. In the model, the velocity of the front of the mass movement was determined using the video analysis and the optical distance lasers. The front was generally formed by the fastest particles within the granular mass. They thus describe the maximum velocity (v). A comparison with the results from the DEM simulation was thus made using the maximum velocity (v) of the particles. The evaluation of the velocity (v) from the DEM simulation was conducted with the help of a geometrically isolated box. The position of the box is shown in Fig. 11 (right). All particles inside the box were analyzed. In Fig. 11 (left), the velocity (v) up to time 3.05 s was 0 m/s (DEM-velocity). This is because there were no particles inside the box up to time 3.05 s. The line denoted with "DEM-velocity" also shows that the following particles behind the front generally have a lower velocity (v), which confirms the statement that the front exhibits maximum velocity (v). Figure 11 (right) shows the two flow states for the mixture on the front of the rigid barrier at time 3.05 and 3.60 s.

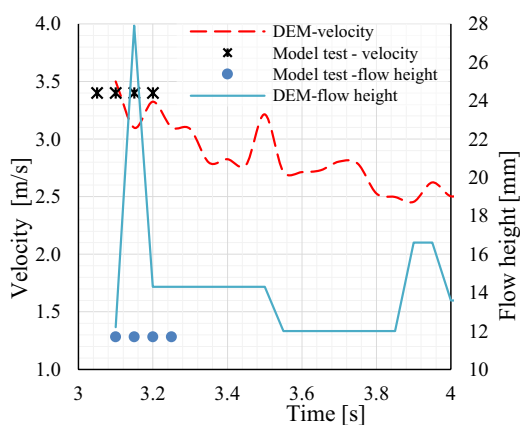


Fig. 11 Left, Comparison of the velocity–time and flow height–time history between the small-scale laboratory experiments and DEM simulation. Right, an illustration of the "Box" with particle positions

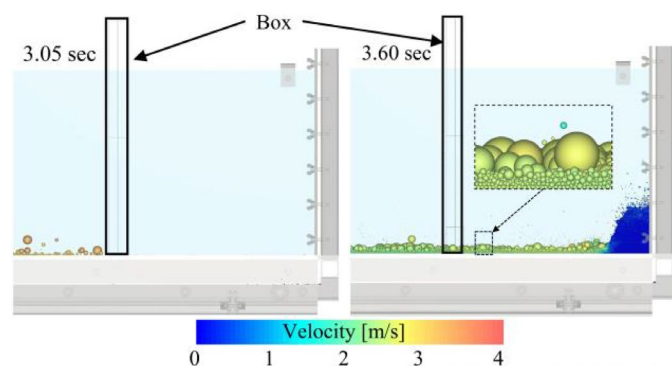
In addition to the velocity (v), the geometric position of the individual particles within the box can be analyzed. If the distance between the particle and the flume base is defined for the analysis, the flow height (h_f) can be determined from the DEM simulation. For comparison, the maximum flow height (h_f) of all particles within the box was examined at each point in time. The results are shown in Fig. 11 (left) as a line labeled "DEM-flow height". The minimum values of the "DEM-flow height" were used for a comparison between the measurement results and the DEM simulation, since individual high-flying particles simulated a flow height (h_f) that was too high. Therefore, the representative flow height (h_f) of the granular mass was 12 mm (Fig. 11, left, "DEM-flow height").

The static or deposition height (h_{stat}) given in Table 5 was between 9.3 cm and 11.2 cm regardless of the type of barrier. The general deposition geometry at or in the barrier was indeed influenced by the deformation of the flexible barrier. Figure 12 shows the deposition height (h_{stat}) in front of the rigid barrier in the DEM simulation and can be compared with Fig. 8. A maximum value of approx. 11.1 cm was reached. The deposition height (h_{stat}) cannot actually be defined by a precisely defined value, since the deposition height according to Fig. 12 was between 9 and 11 cm.

In addition to the deposition height (h_{stat}), inverse grading can be seen in the final state. This effect occurs both in the small-scale laboratory experiment (see Fig. 8) and the DEM simulation. Figure 11 (right) shows that this effect already occurs during the flow process. The larger particles (gravel) float on the smaller particles (sand).

5.2 Deformation Results of the Flexible Barriers

The maximum deformation (f_{max}) of the flexible barriers in the DEM simulation was significantly influenced by the



in the DEM simulation at time steps 3.05 and 3.6 s with a colored scaling denoting the particles' velocity

Fig. 12 Result of the deposition height (h_{stat}) of the mixture in front of the rigid barrier from the DEM simulation. A representation of the mixture at rest at the end of the simulation with inverse grading

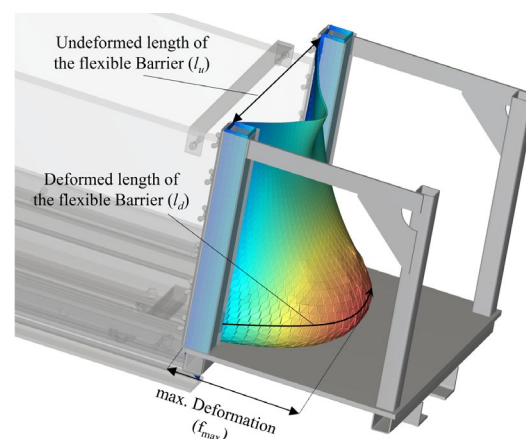
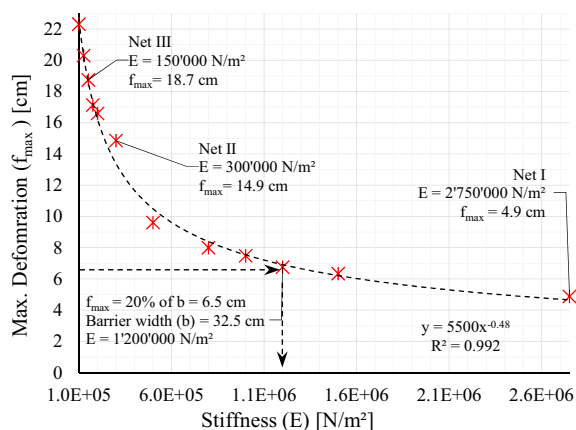
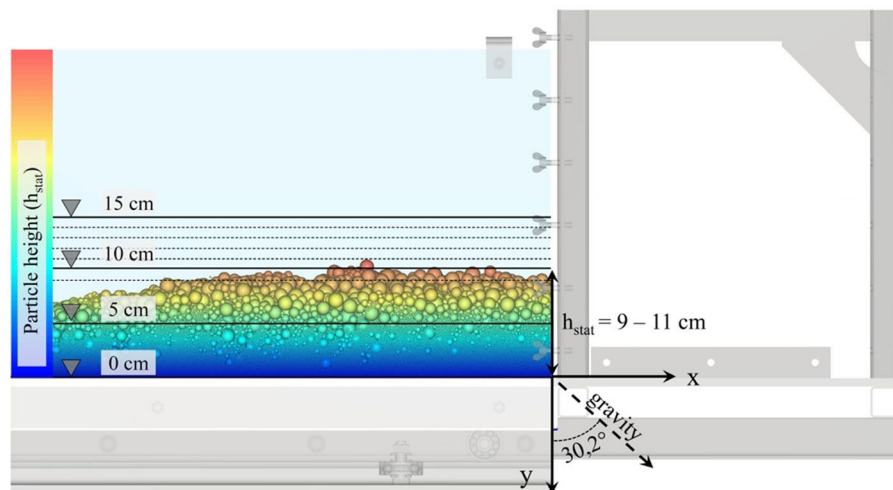


Fig. 13 Left, results of the maximum deformation from the DEM simulation as a function of the stiffness (red stars). An approximation of the results by exponential function with a coefficient of determi-

nation $R=0.992$. Right, flexible barrier in its deformed position with an illustration of the parameters for the max. deformation (f_{max}), the undeformed length (l_u), and the deformed length (l_d)

stiffness (E) used. The definition of the maximum deformation (f_{max}) describes the displacement in the longitudinal direction in the final state (see Fig. 12, x direction) and is also shown in Fig. 13 (right). To investigate the relationship between the maximum deformation and the stiffness for the flexible barriers, DEM simulations with various stiffnesses were carried out. For all calculations, except for the stiffnesses, the same input parameters were used. The number of calculations performed was arbitrary but large enough to describe the relationship between maximum deformation and stiffness. The range of the stiffness (E) was estimated using the tensile tests (see Fig. 6). As a result, 12 DEM simulations were carried out with stiffnesses between $E = 100,000 \text{ N/m}^2$ and $2,750,000 \text{ N/m}^2$. Figure 13 (left) shows the results of the DEM simulations.

The evaluation of the 12 data points in Fig. 13 (left) shows a clear nonlinear relationship between stiffness and

deformation. In addition to the maximum deformation (f_{max}), the deformed length (l_d) of the flexible barrier was also measured at the end of the small-scale model test (see Fig. 13, right). With the undeformed length (l_u) and the deformed length (l_d), the strain ($\epsilon = (l_d - l_u)/l_u$) can be determined. For Net III, the measured strain was approx. 72%. With the results of the tensile test from Fig. 6 and the linear interpolation between the strain of 60 and 80%, a stiffness (E) of $150,400 \text{ N/m}^2$ was calculated. For Net II, a strain (ϵ) of approx. 54% was measured, resulting in a stiffness (E) of $289,000 \text{ N/m}^2$. For Net I, a strain of approx. 20% was measured. This value is not possible for the Net I material (see Fig. 6). In contrast to Net II and Net III, Net I consists of a smooth synthetic net and was pulled out of the lateral fixing by the impact of the granular mass. For this reason, the stiffness (E) chosen for the DEM calculation was the one corresponding to the measured deformation ($f_{\text{max}} = 4.5 \text{ cm}$,

cf. Table 5) of less than 10%. The stiffness for the measured deformation (f_{\max}) according to Table 5 was calculated from the equation of the trend line in Fig. 13, resulting in approx. 2,750,000 N/m². If the stiffnesses were rounded to 50,000 N/m², Net III was assigned a stiffness of $E = 150,000$ N/m², Net II a stiffness of $E = 300,000$ N/m², and Net III a stiffness of $E = 275,000$ N/m². These stiffnesses can therefore be used to compare the maximum deformation (f_{\max}) between the DEM simulation (see Fig. 13) and the measured test results (see Table 5). For the Net III flexible barrier, the deviation between the measured and calculated deformation (f_{\max}) was approx. 6.9%. For the Net II flexible barrier, the deviation in the deformation was 6.4%, while it was 8.9% for Net III. The determination of the maximum deformation using the DEM simulation reached a maximum deviation of less than 10% for all flexible barriers.

With the measured strains and the results of the tensile tests (Fig. 6), the relationship to the load-bearing capacity can be determined. For Net III with a strain of 72%, Fig. 6 shows a load of approx. 8 N, which corresponds to approx. 15% of the load-bearing capacity (52 N). For Net II, with a maximum strain of 54%, a load of approx. 12 N was calculated, which corresponds analogously to approx. 15% of the load-bearing capacity. These low loads in relation to the load-bearing capacity are an essential prerequisite for the use of the elastic material model in Sect. 4. If higher loads are measured in the model tests (especially in the load-bearing capacity range), a material model must be used that can reproduce the non-linear behavior.

5.3 Impact Results Due to the Rigid and Flexible Barriers

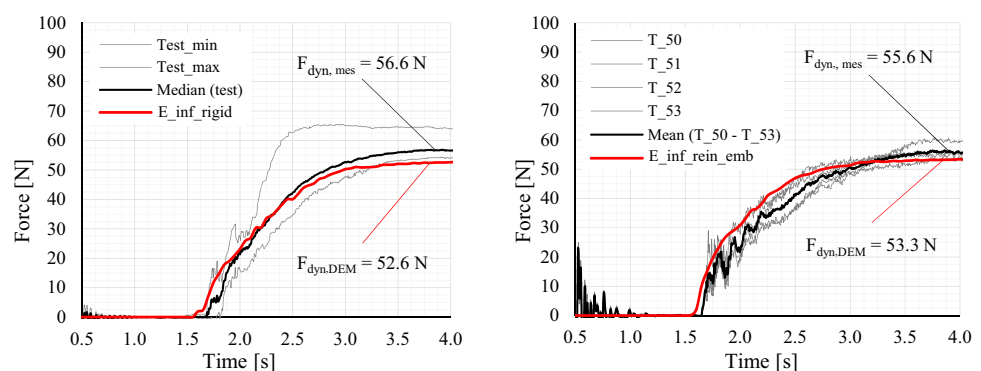
Figure 14 compares the measured results of the force–time history with the results of the DEM simulation. The maximum measured impact in the small-scale laboratory experiment is denoted by $F_{\text{dyn,mes}}$, while it is denoted by $F_{\text{dyn,DEM}}$ for the DEM simulation. The force–time history shown in Fig. 14 on the left shows the comparison between the results of the experiments and the DEM simulation for

the rigid barrier. Figure 14 on the right shows the comparison for the reinforced embankment. If the deviation is related to the maximum dynamic impact force ($F_{\text{dyn,mes}}$ and $F_{\text{dyn,DEM}}$), a difference of approx. 7.6% results when comparing the median of the measured value and the DEM simulation for the rigid barrier. The minimum value ($F_{\text{dyn,mes}}$) from all experiments carried out was 54.2 N with a deviation of 3.0% related to the DEM simulation ($F_{\text{dyn,DEM}}$) for rigid barriers, which was 52.6 N. The calculated dynamic impact force ($F_{\text{dyn,DEM}}$) on the reinforced embankment was 53.3 N with a deviation of 4.1% from the mean value from the experiments ($F_{\text{dyn,mes}}$). In Fig. 14 (left), for the rigid barrier, the minimum values are labeled "Test_min", the maximum values "Test_max", and the median values "Median(test)". The designation "E_inf_rigid" indicates the infinite stiffness of the rigid barrier. In Fig. 14 (right), "T_50" to "T_53" denote the results of the experiments for the reinforced embankment. Analogous to the rigid barrier, the designation "E_inf_rein_emb" indicates the infinite stiffness of the reinforced embankment.

The DEM simulation of the flexible barriers Net I, Net II, and Net III was carried out with the stiffness (E) from Fig. 13 (left). For Net I, a stiffness (E) of 2,750,000 N/m² was used; for Net II, 300,000 N/m²; and for Net III, 150,000 N/m². In Fig. 15 (left), T_36, T_37 and T_38 indicate the results of the experiment with the Net I flexible barrier. In Fig. 15 (middle), the test results are labeled T_30, T_31, and T_32 and refer to Net II. In Fig. 15 (right), the results of the experiment of the Net III flexible barrier are labeled T_39, T_40 and T_41. The red line in all three force–time histories in Fig. 15 shows the result of the DEM simulation. The designation of the DEM simulation in Fig. 15 indicates the stiffness (E) used in N/m².

The deviation of the maximum impact force (F_{dyn}) between the DEM simulation ($S_{\text{dyn,DEM}}$) and the mean value from the experiments ($F_{\text{dyn,mes}}$) was 12.5% for Net I, 2.4% for Net II and approx. 9.1% for Net III. When considered across all flexible barriers, the average deviation was approx. 8%.

Fig. 14 Comparison of the force–time history between the results of the small-scale laboratory experiments and the DEM simulation. Left, evaluation for the rigid barrier; right, evaluation for the reinforced embankment, adapted from (Hofmann and Berger 2022). The term E_inf in "E_inf_rigid and E_inf_rein_embank" denotes an infinite stiffness of the barriers



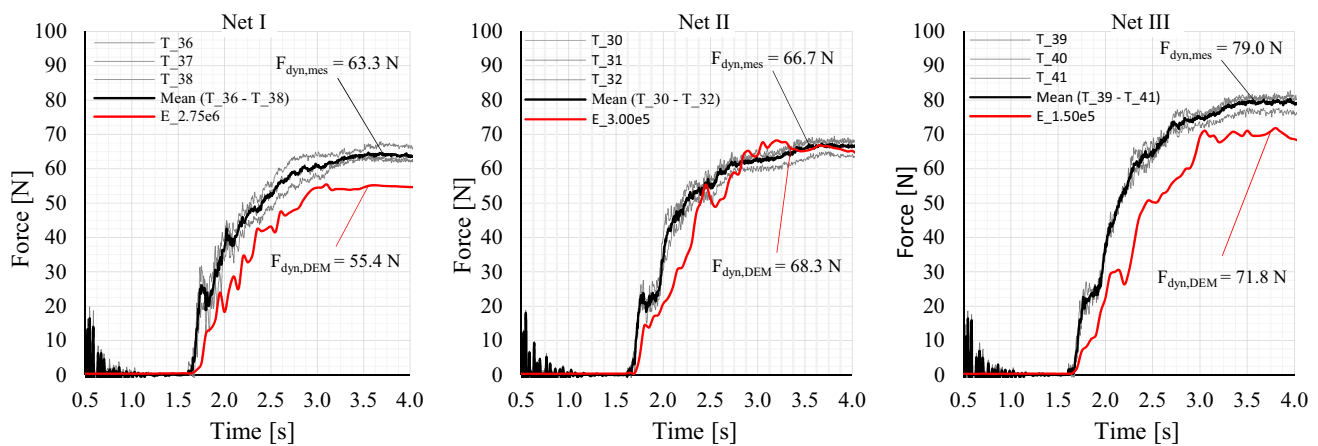


Fig. 15 Comparison of the force–time history between the results of the experiments and the DEM simulation. Left, evaluation for Net I; middle, for Net II; and right, for Net III, adapted from Hofmann and Berger (2022). The gray lines represent the results of the experiments.

The black line represents the mean value of the experiments, and the red lines are the results of the DEM simulation. The designations $E_{2.75e6}$, $E_{3.00e5}$, and $E_{1.50e5}$ refer to the used stiffness in N/m^2 for the DEM simulation

6 Discussion

The comparison of the results from the model experiments and the DEM simulation generally shows good agreement for the front velocity. From Figs. 14 and 15, it can be seen that the impact of the front particles on the barriers corresponds well with the impact of the granular mass in the model experiments. This general observation suggests that the velocity (v) or the increase in velocity (\dot{v}) after opening the gate agrees with the measured values from the experiments. The deviation between the mean velocity from the small-scale laboratory experiment ($v = 3.4$ m/s) and the velocity from the DEM simulation ($v = 3.5$ m/s) amounts to 0.1 m/s. Figure 11 also shows that the velocity (v) within the box decreases steadily. This observation can only be determined for the DEM simulation. The measurement of the velocity (v) in the experiment is carried out exclusively for the front of the granular mass. The evaluation of the flow height (h_f) from the DEM simulation is strongly influenced by individual particles within the box. This generally leads to higher values for the flow height (h_f). For this reason, the minimum values from the "DEM-flow height" curve in Fig. 11 were used for the comparison. The flow height (h_f) was 12.0 mm (see Fig. 11, left) in the DEM simulation, approx. 2.6% above the mean value measured in the experiment. The evaluation assumes that the flow height is constant over time. If the front has a greater flow height than the following part of the mass movement, the flow height can be evaluated according to (Albaba et al. 2015).

Figure 11, right, shows the dead zone, where the particles are at rest. The impact (F_{dyn}) for the rigid barrier and reinforced embankment construction in the DEM simulation resulted in maximum deviations of 7.6% from the measured

values of the experiments. The nonlinear increase in the force–time behavior in Figs. 14 and 15 could be reproduced in the DEM simulation for all barrier types. This behavior results from the velocity reduction for the following particles after the front, as well as from the formation of a dead zone (area of particles with a velocity equal to zero) in front of the barriers and the limited mass with 25 kg. From the tensile tests carried out on the flexible barrier material (Fig. 6), it is clear that there was a non-linear relationship between force and strain. However, the force–strain behavior of the real flexible barriers or a flexible net system was not an easy quantity to determine. The system, the installation itself, and the impact all determine the elasticity response of the protective structure. For this reason, the deformation (f_{max}) was first examined for the DEM simulation using various stiffnesses (E). The stiffness (E), which was determined for Net I, Net II, and Net III, was then used as a calculation in the DEM simulation. For all three flexible barriers (Net I, Net II, and Net III), this resulted in a maximum deviation of $f_{\text{max}} = 8.9\%$. In addition to determining the maximum deformation (f_{max}) as a function of the modulus of elasticity (E), the maximum impact (F_{dyn}) was investigated for different stiffnesses (E). Figure 16 shows the maximum forces (F_{dyn}) as a function of the stiffness of the barrier. Both the measurement results from the experiments and the DEM simulation showed that a more flexible behavior of the protective structure leads to higher forces. A major cause for the occurrence of higher forces is certainly due to the deposition of the granular mass within the flexible barriers. In contrast, for rigid barriers, the entire granular mass is in front of the barrier and not inside it. For extrapolation to real structures, dimensionless indices (e.g., deformation as a function of barrier width, see Fig. 16) can be used to define the limit

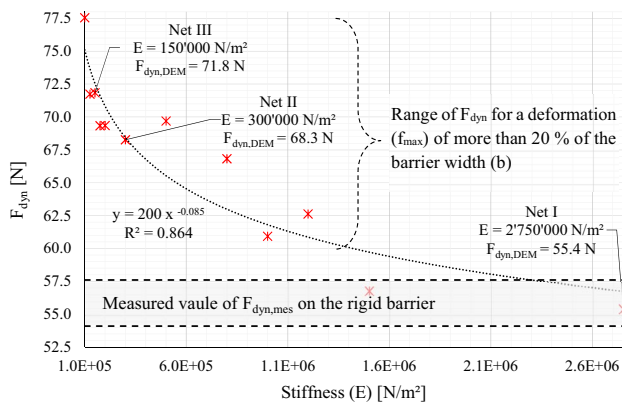


Fig. 16 Results of the maximum impact force (F_{dyn}) from the DEM simulation as a function of the stiffness (red stars). An approximation of the results using an exponential function with a coefficient of determination $R = 0.864$

values. If these limits are exceeded, an increased load on the barrier should then be considered.

The exponential trend line in Fig. 16 ($y = 200 \times (-0.085)$) shows that the lower limits of the rigid barrier were reached when increasing the stiffness of the barrier. These conclusions regarding the maximum dynamic impact force (F_{dyn}) and flexibility of the barrier are limited to impacts due to the highly fragmented granular movements of the several hundred thousand particles. The derivation of this relationship, thus, requires sufficient fragmentation and cannot be applied to individual impacts such as rockfall. Table 8 shows a summary of the results and the deviation between the model experiments and the DEM simulations.

The results of Table 8 and the DEM simulation show that in Eqs. 1 and 2, a parameter becomes necessary to take into account the type of barrier (Hofmann and Berger 2022). The comparison between the individual barrier types focuses mainly on the force–time and force–deformation behaviors. If the maximum dynamic impact force (F_{dyn}) on a protective structure is defined as the decisive load for dimensioning, flexible barriers (see Figs. 9, 14, and 15) were found to experience a higher dynamic impact force (F_{dyn}) than rigid barriers. The global balance of forces is distributed between the barrier and the channel base. The channel base corresponds to the uphill terrain in real events. In contrast to rigid barriers, the granular material of flexible barriers shifts further into the barrier. This reduces the load on the flume base but increases the load on the flexible barrier. While the deformations of the rigid barriers and the reinforced embankment can be considered negligible, these two types differ, particularly in terms of the incline of the impacts. The difference in the inclination of the impact surface between the rigid and the embankment was approx. 20° and hardly had any influence on the maximum dynamic impact (F_{dyn}). The deviation in the measured maximum dynamic impact force ($F_{dyn,mes}$) of the mean values carried out with the small-scale laboratory experiments was less than 4% between the rigid barrier and the reinforced embankment (cf. Table 4). For all the model tests presented here, regardless of the type of barrier, no peak in the impact was measured (force–time curve).

Table 8 Summary of the comparison of the results from the small-scale model experiments and the DEM simulations

Physical parameters	Designation	Unit	Result from experiments	Results from DEM simulation	Deviation
Flow characteristics of the granular mass					
Velocity	(v)	[m/s]	3.4	3.5	2.9%
Flow depth	(h_f)	[mm]	11.7	12.0	2.6%
Deformation of the flexible barrier					
Net I	(f_{max})	[cm]	4.5	4.9	8.9%
Net II	(f_{max})	[cm]	14.0	14.9	6.4%
Net III	(f_{max})	[cm]	17.5	18.7	6.9%
Dynamic impact force F_{dyn}					
Rigid	(F_{dyn})	[N]	56.6 ^a /57.6 ^b	52.6	7.6% ^a /8.7% ^b
Flexible					
Net I	(F_{dyn})	[N]	63.3	55.4	12.5%
Net II	(F_{dyn})	[N]	66.7	68.3	2.4%
Net III	(F_{dyn})	[N]	79.0	71.8	9.1%
Embankment	(F_{dyn})	[N]	55.6	53.3	4.1%

^aMedian value

^bMean value

7 Conclusions

In this study, the results from small-scale laboratory experiments made at the University of Innsbruck were used to investigate the effects of impacts on different barrier types (rigid, flexible, and reinforced embankments). A major advantage of conducting small-scale laboratory experiments is that the boundary conditions of the impact process are the same for all barrier types. In addition to the impact in the force–time history, the velocity (v), flow height (h_f), and deformation of the flexible barriers were determined. A numerical model based on the discrete element method (DEM) was created for the different barrier types. The material parameters for each component, such as the granular material (mixture), flume base, or barriers, were determined in the laboratory. The flow parameters, velocity (v) and flow height (h_f), calculated with the numerical DEM simulation showed maximum deviations of less than 3% in relation to the results from the experiments. The determination of these flow parameters using the discrete element method is, thus, very well suited for calculating the process of fragmented rock avalanches. The stiffness of real flexible barriers is a very complex interaction of different components. System components, such as steel supports, horizontal and uphill guy ropes, braking elements, and different types of nets, are used. If braking elements with large elongations are used, the deflection of the nets increases significantly. In addition to the system components, the human factor must also be taken into account. Due to the non-simultaneous installation of guy ropes, they can be pre-tensioned differently. To counteract this, approval of net systems are based exclusively on real scale tests (EOTA EAD 340059-00-0106 2018). The stiffness (E) of the flexible barrier was determined from the tensile tests (Fig. 6) and deformations (f_{\max}) in the final state from the small-scale model tests. When the maximum dynamic impact force (F_{dyn}) was used as a parameter for a comparison between the DEM simulation ($F_{\text{dyn,DEM}}$) and the mean values of the experiments ($F_{\text{dyn,mes}}$), the deviation of all barrier types was approx. 7.1%. In addition to the comparison of the different dynamic impact forces ($F_{\text{dyn,mes}}$, $F_{\text{dyn,DEM}}$), the use of an elastic material model for flexible barriers can be justified by the fact that the differences between the calculated and measured deformations (f_{\max}) did not differ by more than 8.9% for all flexible barriers. A prerequisite for the use of an elastic material model is low stress in relation to the load-bearing capacity. Both the small-scale laboratory experiment and the DEM simulation showed that the maximum impact (F_{dyn}) also depends on the type of barrier. Highly fragmented granular mass movements demonstrated up to 40% higher loads on flexible barriers. The DEM simulations

with different stiffnesses (E) showed how sensitive the system is with respect to flexibility. Both the deformation (f_{\max}) and the maximum dynamic impact force (F_{dyn}) showed a non-linear relationship. According to Ashwood and Hungr (2016), it was assumed that too much flexibility leads to a higher impact. A large degree of flexibility is cited as a prerequisite. This statement by Ashwood and Hungr (2016) can be confirmed and further specified by the present work. If the deformation (f_{\max}) is more than 20% of the width (b) of the flexible barrier, the influence on the action must be taken into account (Fig. 16). Based on the comparative calculations carried out in Berger and Hofmann (2022), the conclusions and observations can also be applied to real events. With the model experiment from the University of Innsbruck, various questions have been raised concerning gravitational dry mass movements. A total of approx. 200 model experiments were carried out here. In addition to the impacts and flow properties, the runout areas of rock avalanches were also investigated. The numerical DEM simulations serve to examine the test results for plausibility and sensitivity. If a calibrated DEM simulation is generated, various influencing parameters can be investigated, and, thus, parameter studies can be subsequently carried out.

Acknowledgements The computational results (DEM-Simulation) presented here were achieved (in part) using the LEO HPC infrastructure at the University of Innsbruck.

Funding Open access funding provided by University of Innsbruck and Medical University of Innsbruck. Open access funding was provided by the Vice Rectorate for Research at the University of Innsbruck.

Declarations

Conflict of interest The authors declare that they have no conflicts of interest.

Open Access This article is licensed under a Creative Commons Attribution 4.0 International License, which permits use, sharing, adaptation, distribution and reproduction in any medium or format, as long as you give appropriate credit to the original author(s) and the source, provide a link to the Creative Commons licence, and indicate if changes were made. The images or other third party material in this article are included in the article's Creative Commons licence, unless indicated otherwise in a credit line to the material. If material is not included in the article's Creative Commons licence and your intended use is not permitted by statutory regulation or exceeds the permitted use, you will need to obtain permission directly from the copyright holder. To view a copy of this licence, visit <http://creativecommons.org/licenses/by/4.0/>.

References

- Albaba A, Lambert S, Nicot F, Chareyre B (2015) Relation between microstructure and loading applied by a granular flow to a rigid wall using DEM modeling. *Granul Matter* 17(5):603–616

- Albaba A, Lambert S, Kneib F, Chareyre B, Nicot F (2017) DEM modeling of a flexible barrier impacted by a dry granular flow. *Rock Mech Rock Eng* 50:3029–3048
- Albaba A, Lambert S, Faug T (2018) Dry granular avalanche impact force on a rigid wall: analytic shock solution versus discrete element simulations. *Phys Rev E* 97(5):052903
- Ashwood W, Hungr O (2016) Estimating total resisting force in flexible barrier impacted by a granular avalanche using physical and numerical modeling. *Can Geotech J* 53(10):1700–1717
- Berger S, Hofmann R (2022) Impacts on protective structures against gravitational mass movements—scaling from model tests to real events. *Geosciences* 12(7):278
- Bugnion L, McArdell BW, Bartelt P, Wendeler C (2012) Measurements of hillslope debris flow impact pressure on obstacles. *Landslides* 9(2):179–187
- Cagnoli B (2021) Stress level effect on mobility of dry granular flows of angular rock fragments
- Campbell C, Brennen C (1985) Chute flows of granular material: some computer simulations. *SME J Appl Mech* 52:172–178
- Canelli L, Ferrero AM, Migliazza M, Segalini A (2012) Debris flow risk mitigation by the means of rigid and flexible barriers—experimental tests and impact analysis. *Nat Hazards Earth Syst Sci* 12(5):1693–1699
- Cao J, Ahmadi G, Massoudi M (1996) Gravity granular flows of slightly frictional particles down an inclined bumpy chute. *J Fluid Mech* 316:197–221
- Cundall PA, Strack OD (1979) A discrete numerical model for granular assemblies. *Geotechnique* 29:47–65
- Cundall PA (1971) A computer model for simulating progressive large scale movements in blocky rock systems. In: *Proceedings symposium int. soc. rock mech., Nancy Metz, vol 1, S. Paper II–8*
- Daido A (1993) Impact force of mud-debris flows on structures. In: *Proceedings of the congress-international association for hydraulic research, vol 3, pp 211–211. Local organizing committee of the XXV Congress*
- EOTA EAD 340059-00-0106 (2018) Falling Rock Protection Kits. EOTA European Organisation for Technical Approvals
- ESSS Rocky (Release 2022 R1.2) (2022) DEM Technical Manual, ESSS. Rocky DEM, S.R.L.
- Gariano SL, Guzzetti F (2016) Landslides in a changing climate. *Earth Sci Rev* 162:227–252
- Gobiet A, Kotlarski S, Beniston M, Heinrich G, Rajczak J, Stoffel M (2014) 21st century climate change in the European Alps—a review. *Sci Total Environ* 493:1138–1151
- Hofmann R, Berger S (2022) Impacts of gravitational mass movements on protective structures—rock avalanches/granular flow. Basel, Switzerland: *Geosciences* 12(6):223
- Hungr O (2008) Simplified models of spreading flow of dry granular material
- Hungr O, Morgan G, Kellerhals R (1984) Quantitative analysis of debris torrent hazard for design of remedial measures. *Can Geotech J* 21:663–667
- Jiang YJ, Towhata I (2013) Experimental study of dry granular flow and impact behavior against a rigid retaining wall. *Rock Mech Rock Eng* 46:713–729
- Jiang YJ, Fan XY, Li TH, Xiao SY (2018) Influence of particle-size segregation on the impact of dry granular flow. *Powder Technol* 340:39–51
- Lambert S, Bourrier F, Ceron-Mayo AR, Dugelas L, Dubois F, Piton G (2023) Small-scale modeling of flexible barriers. I: Mechanical similitude of the structure. *J Hydraul Eng* 149(3):04022043
- Li X, Zhao J, Soga K (2021) A new physically based impact model for debris flow. *Géotechnique* 71(8):674–685
- Liu C, Yu Z, Zhao S (2020) Quantifying the impact of a debris avalanche against a flexible barrier by coupled DEM-FEM analyses. *Landslides* 17:33–47
- Matuttis H, Chen J (2014) Understanding the discrete element method: simulation of non-spherical particles for granular and multi-body systems. Wiley, New York
- Moriguchi S, Borja RI, Yashima A, Sawada K (2009) Estimating the impact force generated by granular flow on a rigid obstruction. *Acta Geotech* 4(1):57–71
- Ng CW, Choi CE, Song D, Calvello M, Kwan JS, Wang G (2017) Interaction of debris flow with rigid and flexible barriers: centrifuge and numerical simulations. In: *TC1 workshop on advances in landslide understanding*
- Ng CW, Majeed U, Choi CE, De Silva WA (2021) New impact equation using barrier Froude number for the design of dual rigid barriers against debris flows. *Landslides* 18(6):2309–2321
- ONR 24800 (2009) *Schutzbauwerke der Wildbachverbauung—Begriff und Ihre Definitionen sowie Klassifizierung*. Austrian Standards Institute
- ONR 24801 (2013) *Schutzbauwerke der Wildbachverbauung—Statische und dynamische Einwirkungen*. Austrian Standards Institute
- ONR 24802 (2011) *Schutzbauwerke der Wildbachverbauung—Projektierung, Bemessung und konstruktive Durchbildung*. Austrian Standards Institute
- ONR 24810 (2021) *Technical protection against rockfall—terms and definition, effects of actions, design monitoring and maintenance*. Austrian Standards Institute
- Poudyal S, Choi CE, Song D, Zhou GG, Yune CY, Cui Y, Strouth A (2019) Review of the mechanisms of debris-flow impact against barriers. *Association of Environmental and Engineering Geologists; special publication, p 28*
- Preh A (2020) Falls relevant to rock slopes: Runout evaluation by means of numerical models. *Geomech Tunnel* 13(1):59–73
- Proske D, Hübl J, Suda J, Kaitna R, Scheidl C (2011) Debris flow impact estimation for breakers. *Georisk* 5(2):143–155
- Roth W (2003) *Dreidimensionale numerische Simulation von Felsmassenstürzen mittels der Methode der Distinkten Elemente (PFC)*. Vienna University of Technology, PhD Dissertation
- Vagnon F, Segalini A (2016) Debris flow impact estimation on a rigid barrier. *Nat Hazards Earth Syst Sci* 16(7):1691–1697
- VanDine DF (1996) Debris flow control structures for forest engineering. *Work. Pap, 8, 1996.: Res. Br., BC Min. For., Victoria*
- Volkwein A (2005) Numerical simulation of flexible rockfall protection systems. *Comput Civ Eng* 179:122–122
- Wendeler C, Volkwein A, McArdell BW, Bartelt P (2019) Load model for designing flexible steel barriers for debris flow mitigation. *Can Geotech J* 56(6):893–910

Publisher's Note Springer Nature remains neutral with regard to jurisdictional claims in published maps and institutional affiliations.